Journal of Magnetism and Magnetic Materials 436 (2017) 21–30

Contents lists available at ScienceDirect

Journal of Magnetism and Magnetic Materials

journal homepage: www.elsevier.com/locate/jmmm

Research articles

Electron spin resonance in $Cu_{1-x}Fe_xCr_2Se_4$ nanoparticles synthesized with the thermal decomposition method

I.S. Edelman [a,*], S.M. Zharkov [a,b], A.I. Pankrats [a,b], A.M. Vorotynov [a], V.I. Tugarinov [a], R.D. Ivantsov [a], D.A. Petrov [a], D.A. Velikanov [a,b], Chun-Rong Lin [c,*], Chin-Chang Chen [c], Yaw-Teng Tseng [c], Hua-Shu Hsu [c]

[a] Kirensky Institute of Physics, Federal Research Center KSC, Russian Academy of Sciences, Krasnoyarsk 660036, Russia
[b] Siberian Federal University, Krasnoyarsk 660041, Russia
[c] National Pingtung University, Pingtung City, Pingtung County 90003, Taiwan

ARTICLE INFO

Article history:
Received 20 December 2016
Received in revised form 21 March 2017
Accepted 1 April 2017
Available online 6 April 2017

Prime novelty statement: Electron spin resonance (ESR) in ensembles of the $Cu_{1-x}Fe_xCr_2Se_4$ nanoparticles (x = 0, 0.2, and 0.4) synthesized via thermal decomposition method is studied in comparison with nanoparticles structure and morphology. For x = 0 and 0.2, single crystalline nearly hexagonal thin plates demonstrate the tendency to form long stacks consisted of plates attached to each other "face to face. A number of features in the ESR temperature behavior for the NPs with x = 0 and 0.2 have been revealed. Among them there are the non-monotonous temperature dependence of the resonance field with a kink near 130 K what is consistent with a feature in the NPs magnetization temperature changes. The energy gap in the resonance spectrum depends on the x-value and the type of nanoparticles compacting for measurements. One of the main factors is discussed in order to explain the peculiarities: the coexistence of two types of anisotropy in the $Cu_{1-x}Fe_xCr_2Se_4$ NPs, in-plane shape anisotropy and magnetocrystalline anisotropy with four axes, which decreases strongly with the temperature decrease.

ABSTRACT

In this paper, we present a study of the electron spin resonance (ESR) of nanoparticles (NPs) of $Cu_{1-x}Fe_xCr_2Se_4$ chalcogenides with $x = 0$, 0.2, and 0.4. NPs were synthesized via the thermal decomposition of metal chloride salts and selenium powder in a high-temperature organic solvent. According to the XRD and HRTEM data, the NPs were single crystalline nearly hexagonal plates with the structure close to $CuCr_2Se_4$ (Fd-3m, a = 10.337 Å). For $x = 0$ and 0.2, the NPs tend to form long stacks consisting of the plates "face to face" attached to each other due to the magnetostatic interparticle interaction. Only separate NPs were observed in the case of $x = 0.4$. Peculiarities were revealed in the ESR temperature behavior for the NPs with $x = 0$ and 0.2 consistent with the features in the temperature dependences of the NPs magnetization. The non-monotonous dependence of the resonance field H_{res} on the temperature with a kink near 130 K and the energy gap in the resonance spectrum depending on the type of nanoparticle compacting are the distinct peculiarities. One of the main factors is discussed in order to explain the peculiarities: the coexistence of two types of anisotropy in the $Cu_{1-x}Fe_xCr_2Se_4$ NPs, in-plain shape anisotropy and magnetocrystalline anisotropy with four easy axes, which increases strongly with the temperature decrease.

1. Introduction

Copper-chromium chalcogenide $CuCr_2Se_4$, in general, and $CuCr_2Se_4$ nanoparticles (NPs), in particular, attract considerable attention because of the metal conductivity of this material [1] and the Curie temperature, T_c, which is the highest among spinel chalcogenides. It also displays a large magneto-optical Kerr effect (KE) in the near infrared spectral region [2–4] and has highly spin-polarized characteristics [3,5]. This compound was synthesized, for the first time, by Hahn et al. [6]. Lotgering and Van Stapele [7], and later Nakatani et al. [8] showed $CuCr_2Se_4$ to be the p-type metal ferromagnet with $T_c = 460$ K [7] or 430 K ([8] and later publications) and magnetic moment $M_s = 5.07\ \mu_B$/f.u. at 0 K. Nakatani et al. also carried out the first measurements of the electron spin resonance (ESR) in the bulk $CuCr_2Se_4$ single crystal [8]. They obtained the anisotropy constants K_1 and K_2 from the angular dependence of the resonance field:

* Corresponding authors.
E-mail address: ise@iph.krasn.ru (I.S. Edelman).

http://dx.doi.org/10.1016/j.jmmm.2017.04.006
0304-8853/

$K_1 = -6.9^{*}10^5$ and $K_2 = -0.9^{*}10^5$ erg/cm^3 at 5.1 K (the negative K sign means that the <1 1 1> type crystal axes are the magnetization easy axes in the cubic spinel structure). The temperature increase up to 300 K led to the anisotropy decrease by almost one order of magnitude. In Ref. [9], ESR was investigated in the polycrystalline $CuCr_2Se_4$ samples prepared by the solid-state reaction method [10] in the higher temperature interval 300–450 K, i.e., near the Curie temperature. The analysis of the ESR line width and intensity temperature dependences allowed the authors of Ref. [9] to come to a conclusion that ESR in this compound was due to the localized $3d^3$ electrons of Cr^{3+} ions, and the almost linear broadening of the line width with the temperature decrease was associated with the spin-orbit coupling contribution. An analogous conclusion was made for the ferromagnetic $CuCr_2Te_4$ [11] close in the structure and properties to $CuCr_2Se_4$. The results, on the whole, confirmed the model of ferrimagnetic hybridization between the localized $3d^3$ electrons of Cr^{3+} and delocalized holes in the Te 4p band suggested in Ref. [12]. According to the model, the spins of the localized Cr^{3+} ferromagnetic sub-lattice are directed antiparallel to the spins of the delocalized holes of Te 4p.

Ensembles of $CuCr_2Se_4$ nanometric magnetic particles are of particular interest [13]. The static magnetic properties of $CuCr_2Se_4$ NPs synthesized by the solution-based solve-thermal [14–21] and microwave [22] methods were investigated in dependence on the particle size and morphology. In particular, the magnetic properties of $CuCr_2Se_4$ NPs of approximately cubic shape were investigated in Ref. [19,20] as a function of their size of 15–30 nm, and the magnetic moment of the nanocrystals, as well as the Curie temperature were shown to be a little lower than that of the bulk material. This effect was primarily attributed to spin canting at the nanocrystals surface.

Substituting Cu by other transition metals: Co [23], Ni [24], or Fe [25] resulted in the strong changes of the chalcogenide crystal structure and magnetic properties. For instance, in the case of $Cu_{1-x}Fe_xCr_2Se_4$, one of the extreme members of the series – $CuCr_2Se_4$ has a normal spinel structure [26] and is characterized by the ferromagnetic order below ~430 K, as it was mentioned above, while the other extreme member $FeCr_2Se_4$ has the monoclinic structure of the NiAs type [27] and possesses the antiferromagnetic order below 218 K [28,20]. The authors of Refs. [26,15] showed that $Cu_{1-x}Fe_xCr_2Se_4$ bulk compounds crystallized with the spinel structure for $0 \le x \le 0.6$ and with a monoclinic structure for $0.9 \le x \le 1$. For $0.6 < x < 0.9$, the two phases coexisted. They also showed that the charge states of the iron ions were ferric (3^+) and ferrous (2^+) in the spinel and monoclinic structures, respectively, and that the ferromagnetic super-exchange interactions dominated in the spinel phase, while the antiferromagnetic super-exchange interactions dominated in the monoclinic phase.

Recently, we have presented, possibly for the first time, the electron microscopy study and static magnetic properties of the $Cu_{1-x}Fe_xCr_2Se_4$ ($x = 0$, 0.2, and 0.4) NPs synthesized with the thermal decomposition method [29] and revealed some peculiarities in the NPs morphology and magnetization temperature dependences for the compositions with $x = 0$ and 0.2. Besides, the difference between the NPs with $x = 0$ and 0.2, on the one hand, and NPs with $x = 0.4$, on the other hand, was observed. Here, we have undertaken an in-depth study of the ESR in the $Cu_{1-x}Fe_xCr_2Se_4$ NPs, since the data are not available in the current literature. As concerns the nanoparticle morphology and space distribution, we have obtained more accurate transmission electron microscopy data using the goniometric measurements and have revealed the formation of the ordered NPs conglomerates, namely, the stacks of the "face-to-face" oriented thin hexagonal plates which affects the magnetization and ESR temperature dependences of the $Cu_{1-x}Fe_xCr_2Se_4$ NP ensembles for $x = 0$ and 0.2.

2. Experimental

2.1. Synthesis procedure

The nanoparticle fabrication method was described in [29]. To synthesize powdered samples, a mixture of the appropriate amounts of CuCl, $FeCl_2{\cdot}4H_2O$, $CrCl_3{\cdot}6H_2O$ and oleylamin (OLA) was heated at 150 °C for 10 min, and then cooled down to room temperature. Separately, Se powder was dissolved in OLA at 330 °C for 1 h and cooled down to room temperature. The Cu-Fe-Cr-OLA complexes were poured into the Se-OLA complexes and the resulting mixture was heated up to 200 °C and maintained at this temperature for 2 h. Subsequently, the reaction mixture was heated up to 350 °C, and then the temperature of the reaction mixture was decreased to 330 °C and the mixture was aged for 1 h. After the mixture had been cooled down to room temperature, a mixture of hexane and ethanol was added to the solution, so that the products could be separated via centrifugation. To remove the excess of the organic solvent and by-products completely, the products were washed several times with the mixture of hexane and ethanol. The details of the composition of the raw materials for preparing $Cu_{1-x}Fe_xCr_2Se_4$ NPs ($x = 0$, 0.2, and 0.4) are summarized in Table 1.

2.2. Characterization

The crystal structure and phase purity of the samples were characterized by the X-ray powder diffraction (XRD). XRD measurements were performed using Cu Kα radiation, obtained with a rotating-anode X-ray generator operating at 50 kV and 200 mA and a graphite (002) monochromator. XRD patterns were measured at room temperature by step scanning in the angle 2θ range from 10° to 80° with an increment of 0.02°.

The morphology and space distribution of NPs were determined with a high-resolution transmission electron microscope (HRTEM) JEOL JEM-2100 (LaB_6) operating at an accelerating voltage of 200 kV. Selected area electron diffraction (SAED) was used to determine the crystal structure of NPs. Energy dispersive X-ray spectroscopy (EDS) was used for the elemental analysis of the samples.

Magnetization temperature dependences, M(T), were studied with a SQUID magnetometer at temperatures 4.2–450 K in the magnetic field of 200 Oe. The M(T) dependences were recorded in the course of the samples heating after cooling them in one of two different regimes: in the presence of an external magnetic field (FC) and without the magnetic field (ZFC).

The resonance spectra were collected with a Bruker spectrometer (Elexsys E580) operating at X-band (ν = 9.7 GHz) in the temperature range 100–300 K and with a wide band 25–80 GHz magnetic spectrometer with pulse magnetic fields operating at temperatures 4.2–300 K.

3. Results and discussion

3.1. X-ray diffraction studies

The XRD patterns shown in Fig. 1 evidence the presence of the spinel phase, space group Fd-3m, characteristic for $CuCr_2Se_4$ for all three samples of $Cu_{1-x}Fe_xCr_2Se_4$ NPs ($x = 0$, 0.2, and 0.4). No secondary phase is detected. The small shift of the reflexes to lower angles indicates an increase of the lattice constant as compared to the data for $CuCr_2Se_4$ (Fd-3m, lattice constant $a = 10.337$ Å, PDF 4+ card #04-007–5505). Averaged over all the reflections, the lattice constants were a = 10.354, 10.359, and 10.431 Å for $x = 0$, 0.2, and 0.4, correspondingly, i.e., the increase of the lattice

Table 1
Precursor composition used to synthesize $Cu_{1-x}Fe_xCr_2Se_4$ powder. The quantities of the precursor are shown in grams.

Samp.No	x	CuCl	$FeCl_2{\cdot}4H_2O$	$CrCl_3{\cdot}6H_2O$	Se
1	0.0	0.0662	0.0000	0.3560	0.5274
2	0.2	0.0530	0.0266	0.3560	0.5274
3	0.4	0.0396	0.0531	0.3560	0.5274

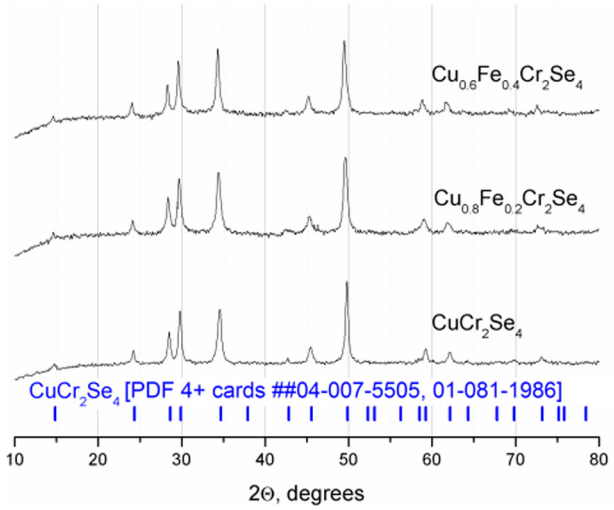

Fig. 1. XRD patterns for three nano-powder $Cu_{1-x}Fe_xCr_2Se_4$ samples (x = 0, 0.2, and 0.4) recorded at the Cu Kα (1.5416 Å) wave length in comparison with the XRD data for the bulk $CuCr_2Se_4$ [PDF 4+ cards ##04-007-5505, 01-081-1986].

constant a was ≈0.2% for $x = 0$ and 0.2, and ≈0.9% for $x = 0.4$. Note, the small lattice constant increase (~1%) was observed for the $CuCr_2Se_4$ NPs of cubic morphology in Ref. [19]. The more noticeable a increase for $x = 0.4$ can be due to the larger Fe^{2+} ion radius (0.78 Å) as compared to the Cu^{2+} ion radius (0.73 Å).

3.2. TEM analysis

The TEM images of samples 1 and 2, shown in Fig. 2a and c, seem to consist of the particles of different morphology: thin nearly hexagonal plates and dark rods. Namely, such interpretation was suggested in our previous work [29]. However, the TEM observation of NPs using a goniometer, i.e., at different tilt angles of the sample, revealed that the particles resembling long dark rods are, in reality, hexagonal plates placed perpendicular to the image plane. An example demonstrating the images of the same region obtained at different tilt angles is shown in Fig. 3. The plates oriented normally to the image (horizontal) plane look like rods. Moreover, they are aggregated into stacks (Fig. 2a, c). The plates in the stacks are located face to face. Sometimes, several stacks can be located close to each other, forming rather large clusters. There is also some amount of solitary hexagonal plates, as well as broken hexagonal, triangular, and rectangular plates. The distances between the atomic planes ≈5.97 Å and 2.98 Å observed in the HRTEM images of samples 1 and 2 (Fig. 1b, d) are characteristic for the (1 1 1) and (2 2 2) planes of the $CuCr_2Se_4$ phase with the spinel structure. This suggests that the (1 1 1) crystallographic plane is the predominant growth plane of the plates. For sample 3, only isolated NPs are observed (Fig. 4). The spot reflections observed in the SAED patterns are consistent with the XRD data.

The thicknesses of the plates were estimated using the HRTEM images of NPs oriented normally to the image plane. The average plate thickness, 2d, was about ~20 nm for samples 1 and 2, and ~10 nm for sample 3. These estimations are close to the average NPs size obtained from the broadening of the XRD reflection (4 4 0): 21–23 nm for $x = 0$ and 0.2, and 18 nm for $x = 0.4$. The XRD reflection broadening is known to be due to the lower size of the non-cubic or the non-spherical NPs. Naturally, in the case of the thin plates their thickness corresponds to the minimal size. The lognormal distributions of the nanoparticle diameters, 2R, are shown in Fig. 5 for all three cases ($x = 0$, 0.2, and $x = 0.4$). The diameters corresponding to the maxima of the distribution curves and the width of the curves are seen to be approximately three times larger for samples 1 and 2 as compared to sample 3. The nanoparticle average diameter, aspect ratio $\tau = d/R$, room temperature magnetization M, and Curie temperature T_c are collected in Table 2. For sample 1 containing no Fe, the Curie temperature was obtained to be equal to 410 K which is lower as compared to the bulk counterpart (430 K for polycrystalline samples prepared by the solid-state reaction method [8,9]), close to T_c of $CuCr_2Se_4$ thin films (405–410 K [30]) and nanocrystals (395–409 K [19]).

3.3. The nanoparticles aggregation and magnetic properties

The tendency of NPs aggregation to more or less extended stacks and larger clusters is, obviously, due to the interparticle interactions, and it should affect the magnetic properties of the whole nanoparticle ensemble. The formation of the magnetic nanoparticle clusters was considered in many works devoted to colloidal nanoparticle systems, where magneto-static interaction affected nanoparticle arrangement in any conglomerates because of their mobility in a liquid (e.g., [31]). In a powder of NPs, the strength of such an interaction can also provide conditions for cluster formation. To estimate the magneto-static interaction energy which results in the formation of the stacks of NPs located face to face to each other, we use the results obtained by M. Beleggia and co-authors [32] who developed a new approach to the calculation of the magneto-static interaction energy between two NPs of an arbitrary shape and magnetization direction. They considered particles with the rotational symmetry: interacting cylinders of variable aspect ratios (disks and rods) and spatial magnetization orientation (in-plane and axial orientations of magnetic vectors). In our case, NPs (hexagonal plates) can be considered as discs with the thickness 2d and diameter 2R. The self-energy of such a solitary cylinder can be expressed, according to [32], as a function of the aspect ratio $\tau = d/R$ and orientation of the vector $\vec{\mu} = \vec{M}\,v$, where $\vec{M}$ is the substance magnetization and v is the volume of the particle. It was shown in [32] that the in-plane magnetization orientation corresponded to the lowest energy of a disc for $\tau < \tau_c \equiv 0.90647$, while for $\tau > \tau_c$ the axial magnetization orientation was preferable. Note, this statement is valid only in the cases when one can neglect the magnetocrystalline anisotropy. In the case of two discs, the interaction energy was shown to depend on the disc arrangement: in one plane or along one axis [32]. The latter configuration, most interesting for us, is presented in Fig. 6a. The interaction energy between two discs in such configuration for magnetic moments oriented in the disc plane was written in [32] as

$$E_v^{int} = \frac{\vec{\mu}_1 \cdot \vec{\mu}_2}{h^3} S_1(\zeta, \tau) \qquad (1)$$

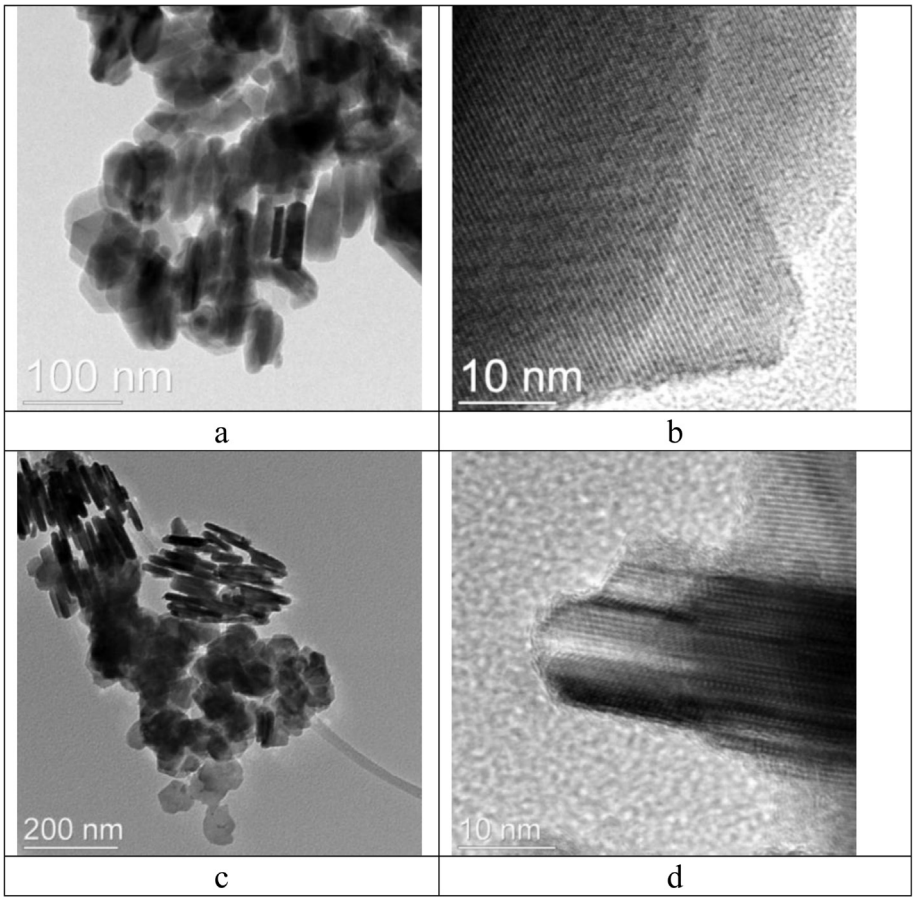

Fig. 2. TEM (a, c) and HRTEM (b, d) images of samples 1 (a and b) and 2 (c and d).

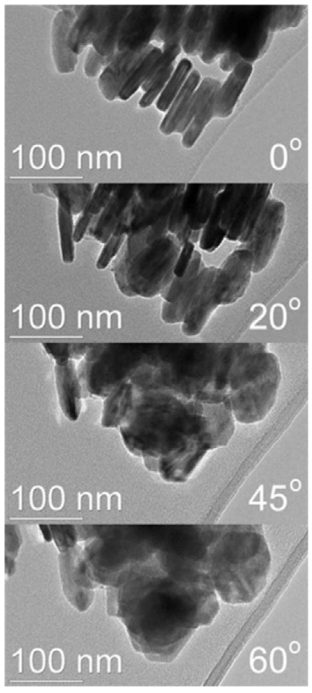

Fig. 3. Series of TEM images (sample 1) obtained from the same area at different tilt angles.

where $\vec{\mu}_i = \vec{M}_i v_i$ and S_1 is the dimensionless function of the geometrical parameters of a system, determined by Eq. (64) in Ref. [32]:

$$S_1(\zeta,\tau) = 8\zeta^3\tau\sum_{n=-1}^{+1} c_n[4+(2\zeta+n)^2\tau^2]^{1/2}\times {}_2F_1\left(-\frac{1}{2},\frac{1}{2};2;\frac{4}{4+(2\zeta+n)^2\tau^2}\right) \quad (2)$$

Here $\zeta = h/d$, $\tau = d/R$, 2h is the distance between the centers of the discs, ${}_2F_1$ is the standard hypergeometric series, and $c_{-1,0,1} = [1,-2,1]$. The authors of Ref. [32] have shown that $S_1 > 0$ and therefore the opposite orientations of the magnetic moments of the neighboring discs provide the lower energy of the system. They have shown also that $S_1(\zeta,\tau) \to 1$ at $\zeta \to \infty$ and, consequently, interparticle interaction can be described by the simple dipolar approximation in this case. However, when the distance between discs decreases, strong deviations from the dipole-dipole interaction appear. The maximal deviations are reached when the discs are in contact with each other, that is, when $h = d$, as it is shown in Fig. 2a and c. The energy minimum for this case is significantly deeper than for dipole approximation. These statements can be generalized for the system with a larger number of the discs, as shown schematically in Fig. 6b, but equations for E^{int} in this case should be different from Eqs. (1) and (2). However, the latter equations qualitatively explain the formation of the long stacks of the planar NPs. Inclusion of the magnetocrystalline anisotropy into consideration may significantly complicate the picture. One of the possible options is shown in Fig. 6c. Such a situation can take place for the $CuCr_2Se_4$ thin plates growing in the (1 1 1) plane, where the shape anisotropy coexists with the magnetocrystalline

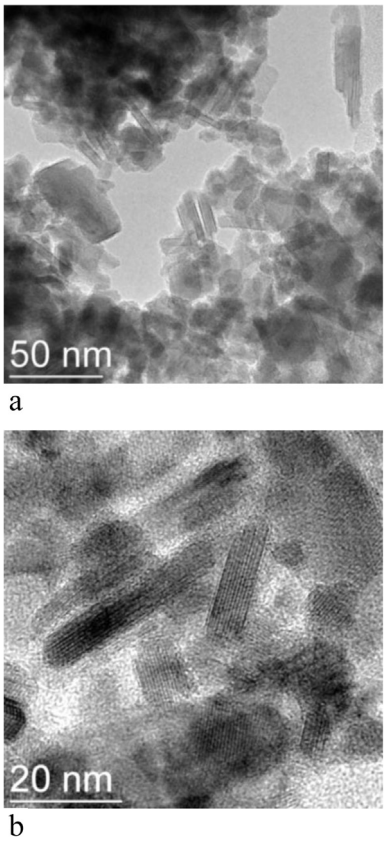

Fig. 4. TEM (a) and HRTEM (b) images of sample 3.

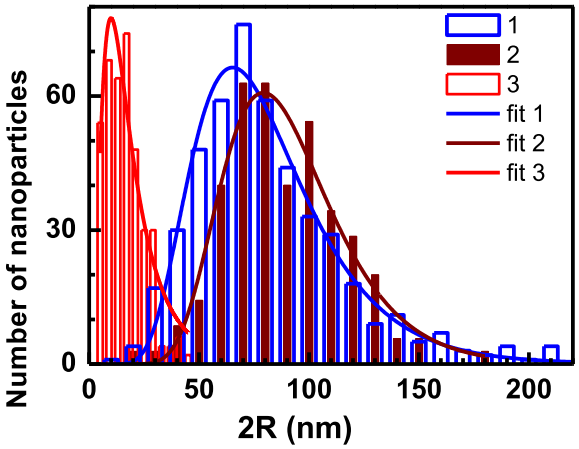

Fig. 5. Nanoparticle diameter, 2R, size distributions and the lognormal fitting for samples 1 (blue), 2 (vine), and 3 (red). (For interpretation of the references to colour in this figure legend, the reader is referred to the web version of this article.)

Table 2
Parameters of NPs (samples 1–3): average diameter 2R, aspect ratio $\tau = d/R$, room temperature magnetization M, and Curie temperature T_c.

Sample No	<2R>, nm	<τ>	M, G (T = 300 K)	T_c, K
1	65	0.34	187	410
2	79	0.28	146	401
3	16	0.44	55	322

anisotropy characterized by four axes (Fig. 6d) of the easy magnetization. Further formation of clusters joining the nanoparticle stacks can also be associated with the magneto-static interaction between the stacks.

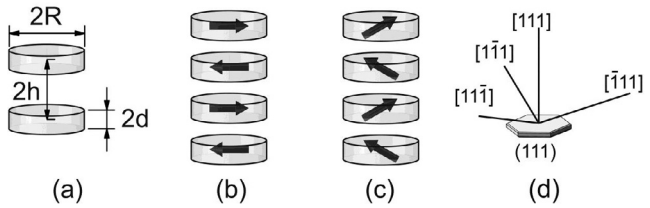

Fig. 6. Scheme of the arrangement of two magnetic discs, according to Ref. [32] (a), possible magnetic vector orientations in a set of disc-shaped NPs situated face-to-face to each other (b, c), and orientations of the magnetocrystalline anisotropy easy axes relative to the (1 1 1) crystal plane (d).

As mentioned above, the nearly hexagonal NPs observed in samples 1 and 2 (Figs. 2 and 3) can be approximated by the discs. Based on the values of the aspect ratio $\tau = d/R$ presented in Table 2, one can expect the magnetic moment of the nanodisks to be directed in their planes at room temperature. The magnetic moments of the neighboring particles in the stacks tend to align in opposite directions according to Eq. (1) forming a structure resembling the domain structure in a crystal. The magnetic moments of the nano-discs can line up identically under the action of the relatively low external magnetic field. The magnetization values (Table 2) were estimated from the FC magnetization temperature dependences shown in Fig. 7 taking into account the saturation magnetization presented in Fig. 6 in Ref. [29]. For sample 1, the magnetization value is close to the magnetization of the epitaxial $CuCr_2Se_4$ film in the external magnetic field of the comparable value [31]. Being guided by the magnetization and the aspect ratio values, one can expect approximately the same interparticle interaction strength for samples 1 and 2. Indeed, in both these samples, the stacks of parallel face-to-face oriented plates are observed. The magnetization and Curie temperature of sample 3 decrease strongly because of the higher iron concentration in the compound. As mentioned in the Introduction, the Cu substitution by Fe in $Cu_{1-x}Fe_xCr_2Se_4$ leads to the appearance of antiferromagnetic super-exchange interaction [15] and, as a consequence, to the decrease of the magnetization and Curie temperature of a sample. Therefore, the magnetostatic interaction between NPs should also be small, and there will be no reason for the formation of their conglomerates.

It is seen from Fig. 7 that for samples 1 and 2, the ZFC and FC magnetization curves bifurcate at temperatures close to T_c. These bifurcation temperatures (or the irreversibility temperatures, T_{irr}) are in good agreement with T_{irr} observed in Ref. [9] for polycrystalline bulk $CuCr_2Se_4$ samples prepared by the solid-state reaction method. The ZFC curves demonstrate very broad non-symmetry peaks with kinks at about 130–140 K (in the magnetic field of 200 Oe). The difference in the temperature behavior of the FC and ZFC modes is typical for the transition from the superparamagnetic to the blocked ("frozen") state in an ensemble of magnetic NPs. The T_{irr} values for samples 1, 2, 3 correlate well with the nanoparticle average dimensions in these samples (see Table 2).

3.4. Electron spin resonance

Typical X-band ESR spectra are presented for two temperatures in Fig. 8 as the first derivatives of absorption. The resonance linewidth, ΔH, and resonance field, H_{res}, were determined as the peak-to-peak distance and center of this distance, respectively (see Fig. 8). At room temperature, the observed spectrum has the line shape close to the Gauss curve. At the temperature lowering, the line shape distorts and looks like an inhomogeneously widened spectrum as it can be seen in Fig. 8 where the best fits of the spectra are shown for the Gauss and Lorentz line shape.

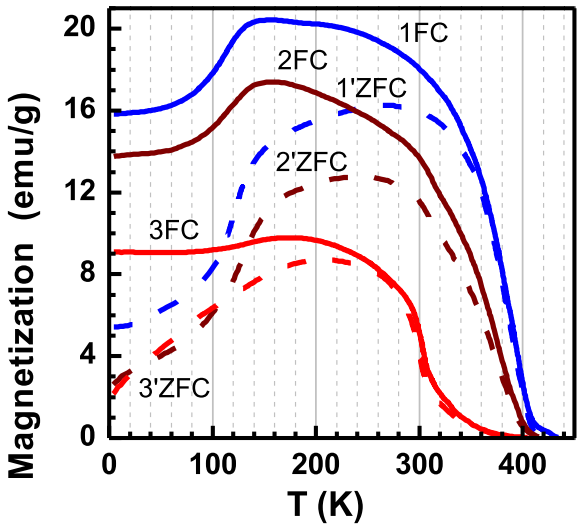

Fig. 7. The FC (solid curves) and ZFC (dashed curves) magnetization temperature dependences of samples 1–3 (curves 1–3, correspondingly). H = 200 Oe.

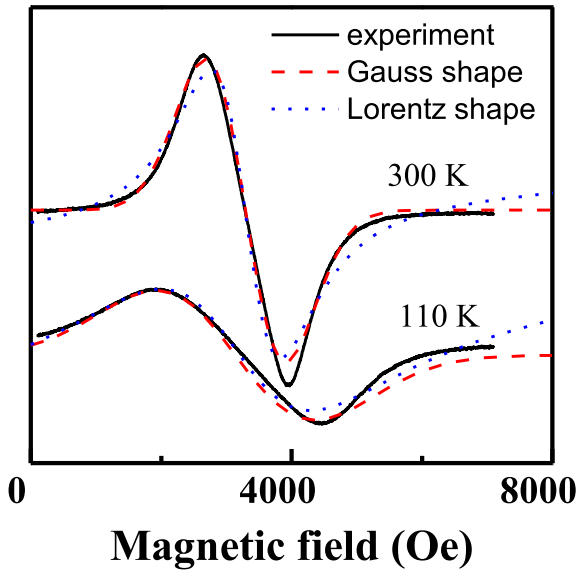

Fig. 8. Derivatives of the experimental resonance absorption line (solid lines) in the X-band of sample 1 and Gauss (puncture) and Lorentz (dashed) fittings at two temperatures.

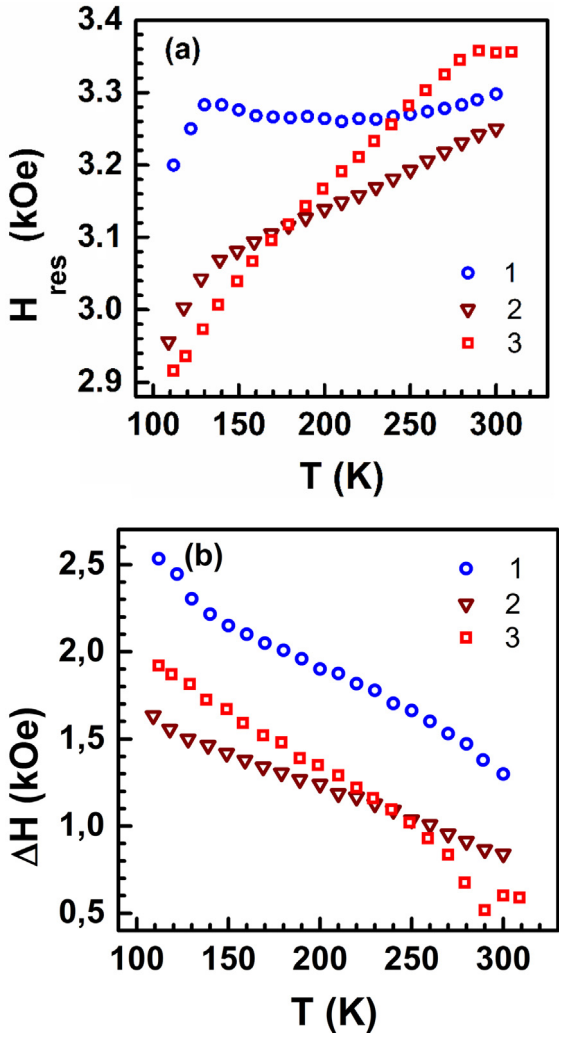

Fig. 9. (a) Temperature dependences of the resonance fields of samples 1–3; (b) Temperature dependences of the line width of samples 1–3.

The character of the resonance field, H_{res}, temperature dependencies (Fig. 9) change with the change of the Fe content in the sample. For sample 1 containing no Fe ions, the H_{res} value is almost constant in the interval 300–140 K. At temperature 130–137 K a kink appears, after which H_{res} diminishes very fast. Such a behavior is markedly different from the permanent reduction of H_{res} with the temperature decrease observed in Ref. [9] for the bulk polycrystalline samples. For sample 2 with $x = 0.2$, H_{res} decreases through the whole temperature interval similar to the bulk sample case [9]. However, a kink is observed at the same temperature 130–137 K, and H_{res} decreases faster after the kink point. The kink is less pronounced in this case. The temperatures of the kink, T_{kink}, correlate with the temperature interval where the features are observed in the thermomagnetic curves (see Fig. 7). The kink and the subsequent H_{res} decrease can evidence the appearance of a gap in the magnetic resonance spectrum. Similar H_{res} behavior was revealed for nano-sized samples $CuCr_2S_4$ [33], where the kink was associated with NPs blocking temperature T_b. The T_{kink} origin in our case will be discussed further.

For sample 3 with higher Fe content, the situation typical for the superparamagnetic particles takes place: H_{res} of this sample is constant at temperatures exceeding ~270 K which coincides approximately with the T_{irr} determined from the magnetization temperature dependence (Fig. 7). At lower temperatures, the shape of the H_{res} (T) curve is similar to that observed in Ref. [9].

The resonance linewidth, ΔH, of all the investigated samples increases with the temperature decrease which is similar, in principle, to the ESR line width temperature behavior of the polycrystalline $CuCr_2Se_4$ sample observed in Ref. [9].

ESR was also investigated in the lower temperature interval using a wide band magnetic resonance spectrometer with the pulse magnetic field. Two variants of the sample preparation for the measurements were used: “free particles” – nanoparticle powder was placed in a thin-walled plastic tube of 2 mm in length and 3 mm in diameter; in the second variant, NPs were mixed with an alcohol solution of the glue and the mixture was solidified (fixed NPs). For the free and fixed particles, the shape of the resonance curves and the resonance characteristic dependences on the temperature are, principally, the same. However, the values of the temperature changes are different for these two cases.

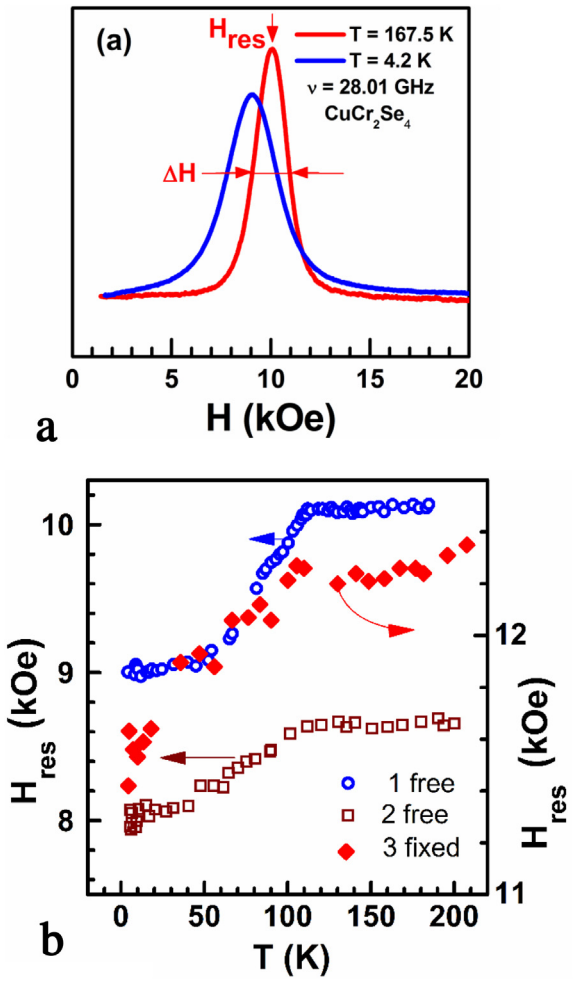

Fig. 10. (a) The resonance spectra of sample 1 measured using a wide band spectrometer at two temperatures; (b) The resonance field, H_{res}, temperature evolution for samples 1 (circles) and 2 (squares) with the free NPs, ν = 28.0 GHz and 25.95 GHz, correspondingly, and for sample 3 with the fixed NPs, ν = 35.07 GHz (diamonds).

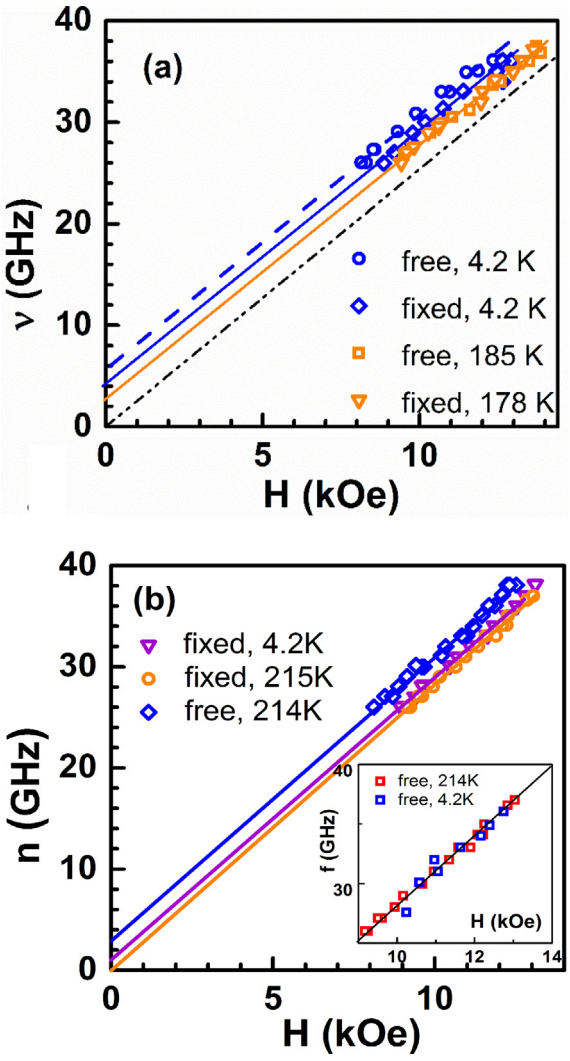

Fig. 11. The frequency-field dependences measured at the temperatures lower (red icons and lines) and higher (blue icons and lines) than T_{kink} of sample 1: (a) for sample 1 and (b) for sample 3. The circles and diamonds refer to the free and fixed NPs, correspondingly. Inset in b: Frequency-field dependences for the free NPs in sample 3 at two temperatures. (For interpretation of the references to colour in this figure legend, the reader is referred to the web version of this article.)

The typical resonance spectra measured for sample 1 at two temperatures using pulse magnetic field are shown in Fig. 10a. Here, we also show how the resonance parameters H_{res} and ΔH were determined in these measurements. The H_{res} temperature evolution for samples 1 and 2 with the free NPs and sample 3 with the fixed NPs are shown in Fig. 10b. An essential difference is seen between samples 1 and 2, on the one hand and sample 3 on the other hand. For samples 1 and 2, beginning with $T_{kink} \sim 110$ K, H_{res} decreases almost monotonously with the temperature decrease and reaches a plateau near ~50 K. In the temperature interval 100–300 K, the curve is similar to that recorded in the X-band. Some T_{kink} diminishing as compared to the measurements in the X-band can be associated, most likely, with the essential increase of the external magnetic field due to the higher resonance frequency of the spectrometer. Note more smooth changes in the shape of the $H_{res}(T)$ curve for sample 2. For sample 3, the monotonous H_{res} decrease is observed in the whole temperature interval used. The difference between the two types of NPs – free and fixed – in samples 1 and 2 is revealed at a lower temperature in the frequency-field dependences (the example is shown in Fig 11a for sample 1) while for sample 3 the frequency-field dependences are the same both in the low and high temperature intervals (Fig. 11b).

For both temperature intervals, the dependences are linear. At low temperature, they demonstrate gaps ν_c with H → 0: ν_c = 5.9 GHz and 4.2 GHz for the free and fixed NPs, correspondingly, in sample 1 (see Fig. 11a), and ν_c = 3.0 GHz for the fixed NPs with the gap being absent in the free ones in sample 3 (see Fig. 11b, Inset). At higher temperatures, the gaps are the same for both types of NPs (2.6 GHz) in sample 1, and the gap practically disappears for sample 3. So, the difference between the free and fixed NPs behavior is noticeable at low temperatures, only. Note that with the lowering temperature, the changes of the energy gap in sample 1 are maximal for free particles. In contrast, the gap is temperature independent for free particles of sample 3 in which the maximal changes are found for the fixed ones. The peculiarities in the temperature and frequency dependences of H_{res} can be caused by different reasons. The crystal magnetic anisotropy can be one of the reasons.

The ESR frequency-field dependences of the blocked superparamagnetic particles should be linear and described by the equation obtained in Ref. [33]:

$$\nu/\gamma = H_{res} + < H_A > \quad (3)$$

where ν is the resonance frequency, γ is the gyromagnetic ratio, and $<H_A>$ is the average value of the anisotropy field. $<H_A>$ determines the energy gap $\nu_c = \gamma<H_A>$ in the resonance spectrum. It is also seen from Eq. (3) that the H_{res} temperature behavior is governed by the anisotropy temperature dependence. The coexistence of two types of anisotropy is characteristic of the samples under investigation: shape and crystalline anisotropy. The shape anisotropy, H_{sh}, of the NPs with the thickness significantly lower as compared to the lateral dimensions is described by the equation

$$H_{sh} = N_\alpha \pi M_s \tag{4}$$

where M_s is the spontaneous magnetization, the form-factor N_α equals to

$$N_\alpha = \frac{1}{1-\tau^2}\left[1 - \frac{\tau}{(1-\tau^2)^{1/2}}\arccos\tau\right] \; at \; \tau = \frac{d}{R} < 1 \tag{5}$$

It is evidenced from (4) and (5) that the H_{sh} temperature dependence is determined by the M_s temperature dependence, only.

The field of the magnetocrystalline anisotropy is equal to

$$H_K = 2K/M_s \tag{6}$$

where K is the magnetic anisotropy constant depending strongly on the temperature in the case of $CuCr_2Se_4$: $K = -6.9^*10^5$ erg/cm^3 at 5 K and $K = -0.9^*10^5$ erg/cm^3 at 290 K [8], i.e., K increases almost one order of magnitude with the temperature lowering from 300 to 5 K.

As it was mentioned above, in $CuCr_2Se_4$ cubic crystal lattice, there are four easy axes of the <1 1 1> type: one orients at an angle of 90° relative to the (1 1 1) crystal plane, i.e., relative to the nanoparticle plane, and three orient at angles 19.471° to this plane (see Fig. 6d). The magnetocrystalline anisotropy, H_K, tends to direct the magnetic moment of each particle along one of the <1 1 1> axes closest to the direction of an external magnetic field. The shape anisotropy, H_{sh}, tends to direct the nanoparticle magnetic moment in the nanoparticle plane. So, in each nanoparticle, the effective anisotropy field will be the vector sum of the shape and magnetocrystalline anisotropy fields, and its direction and value will depend on the temperature. Fig. 12 demonstrates the H_{sh} and H_K temperature dependences calculated using Eqs. (4) and (6) with different values of M_s: curves 1 and 2 correspond to M_s value

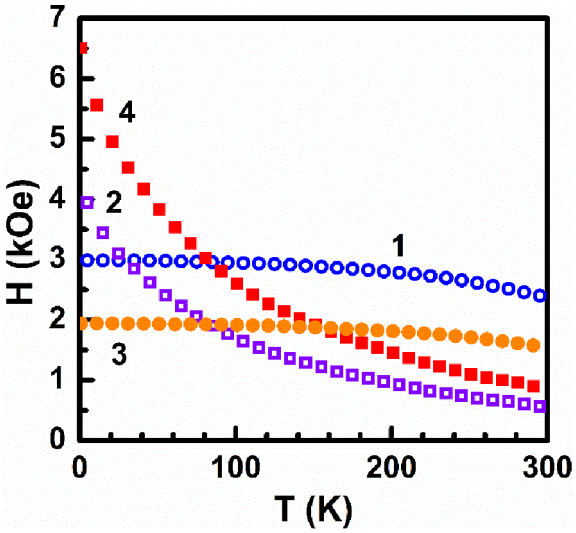

Fig. 12. Temperature dependences of the shape anisotropy, H_{sh}, (curves 1, 3) and magnetocrystalline anisotropy H_K (curves 2, 4) fields calculated according to Eqs. (4) and (5) for sample 1. The M_s value was taken for $CuCr_2Se_4$ from Ref. [8] (curves 1 and 2) and from Table 2 (curves 3 and 4). K1 value was taken from Ref. [8].

presented in Ref. [8], curves 3 and 4 were obtained with M_s of sample 1. It is seen that at higher temperatures H_{sh} prevails which determines the magnetization vector orientation in the nanoparticle plane. At some temperature, curves $H_{sh}(T)$ and $H_K(T)$ intersect, and H_K gives predominating contribution to the effective anisotropy. For the M_s value of the real sample 1, the intersection temperature is close to the kink temperature in Figs. 7, 9a, and 10. The transition from the in-plain magnetization orientation to its orientation at any angle or even perpendicular to the nanoparticle plane can result in the change of the magnetostatic interaction in the nanoparticle stacks. In some temperature interval, the anisotropy increase can be compensated by the interparticle interaction decrease and, as a consequence, H_{res} will be approximately constant in some temperature interval as it is seen in Figs. 9a and 10. A sharp increase in the magnetocrystalline anisotropy at a temperature lower than the intersection point leads to a decrease of H_{res} at further temperature decrease.

No data on the $Cu_{0.8}Fe_{0.2}Cr_2Se_4$ and $Cu_{0.6}Fe_{0.4}Cr_2Se_4$ magnetocrystalline anisotropy are available in literature. However, one can assume a similar increase in the magnetocrystalline anisotropy in these samples, and associate the gradual decrease in the H_{res} value in all the samples with this mechanism. For sample 3 containing only separate NPs, this mechanism can be valid in the whole temperature region investigated as it was revealed in Ref. [33] for an ensemble of separate cubic NPs of the related compound $CuCr_2S_4$.

A different character of the frequency-field dependence of the resonance in the free and fixed NPs can be explained on the basis of Eq. (3). The free particles having a large magnetic moment can be mechanically rotated in the applied magnetic field. Thus, during the resonant measurements, most of the particles will be oriented in the directions close to the axis of easy magnetization. Such a particle orientation provides the maximum value of the averaged anisotropy field $<H_A>$ at the temperatures below blocking and, as a consequence, the greatest value of the gap in Eq. (3). In the case of NPs fixed in the glue in the absence of a magnetic field, NPs orientation relatively to each other remains chaotic providing lower values both of the averaged effective anisotropy field and the energy gap in the resonance spectrum. Namely, such a picture is observed in the case of sample 1 (see Fig. 11a). The averaged effective anisotropy field calculated for sample 1 from the frequency-field dependence shown in Fig. 11a is equal to $<H_A> = 2.1$ kOe at T = 4.2 K, this value is close in the order to the estimated one shown in Fig. 12.

The difference between the free and fixed NPs is also revealed in the temperature dependences of the resonant line width (see Fig. 13). For sample 1, at temperatures above the blocking, the line widths both of the free and fixed NPs are close and increasing slowly with the temperature decrease. The difference appears just below the blocking temperature $T_{kink} \approx 110$ K: the line width for the fixed particles increases with further lowering of the temperature much faster than that for the free particles, it reaches the value of 2.4 kOe at T = 4.2 K while the line width in the free particles is equal to 1.6 kOe at the same temperature. The value of the line width for the fixed particles retaining their chaotic orientation can be estimated in the same manner as for a polycrystalline sample [34]: $\Delta H \approx H_A$, which is close to the averaged value of the effective anisotropy field $<H_A> = 2.1$ kOe determined from the resonance properties. It is obvious that the line width is less when measured in the free particles whose dispersion in the directions of the easy axes of magnetization relative to the direction of the applied field is much smaller.

Since NPs in sample 1 and 2 possess rather high magnetic moment at room temperature, they can be oriented nearly homogeneously by the magnetic field applied in the process of

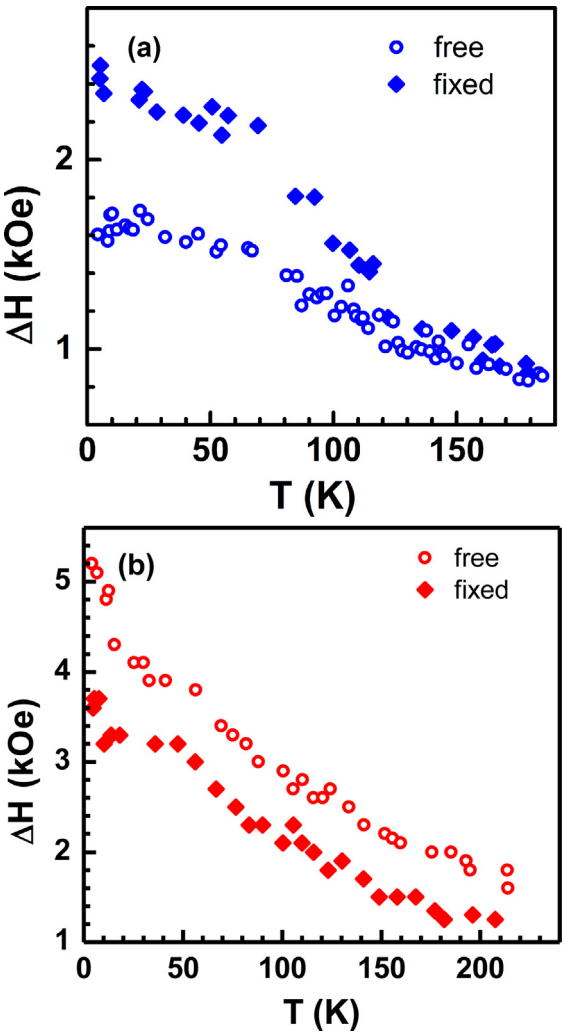

Fig. 13. The line width temperature dependences measured in samples 1 (a) and 3 (b) with the free (circles) and fixed (diamond) NPs.

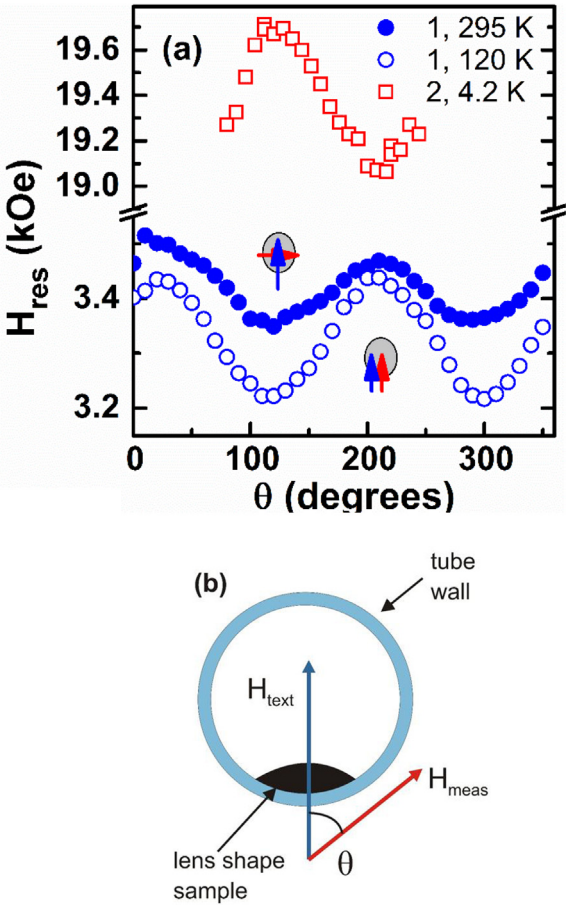

Fig. 14. (a) The H_{res} angle dependences for sample 1 solidified in the magnetic field. Experimental points 1 correspond to the lens shaped sample measured at the frequency 9.7 GHz, points 2 are obtained for the sample of cylindrical shape at 52.66 GHz. (b) Scheme of the experimental procedure.

the sample solidification. Moreover, a texture will appear in the samples and all the easy axes of the particles will be parallel to each other, in preference. We expected the angle dependence of the resonance field with the minima and maxima corresponding to the measurement field orientation parallel and perpendicular, correspondingly, to the direction of the magnetic field applied during the sample preparation. But the real dependences appear to have the opposite character: the minimal resonance fields correspond to the measurement field orientations being perpendicular to the field applied during the sample solidification. It seems likely, that the origin of such an unusual dependence is consistent with the macroscopic anisotropy of the sample shape. The experiment in a high-sensitive X-band spectrometer required a small amount of a sample. The magnetic field of a permanent magnet possessing some inhomogeneity was used to create texture. Thereby, during solidification, the solution with the powder formed a lens-shaped sample collected near the container wall where the magnet pole was placed, as it is shown in Fig. 14b. Indeed, the direction of the texturing magnetic field coinciding with the axis of the lens-shaped sample close to the disk is the hard axis of magnetization. The perpendicular direction lies in the plane of the disk being the easy plane of magnetization. The distinct 180° dependence of H_{res} was observed due to the magnetic shape anisotropy which, as it appears, prevailed over the anisotropy of the magnetic texture and had the opposite sign. The amplitude of the H_{res} (θ) curve increases with the temperature decrease in accordance with the temperature dependence of the magnetization.

We also prepared a sample of cylindrical shape filling the entire volume of the tube to measure it by the wide-band spectrometer. Such a sample has no shape magnetic anisotropy in the plane perpendicular to the axis of the cylinder. In this case (see Fig. 14a), we observed the angular dependence of the resonance field just due to the anisotropy of the magnetic texture with the minima and maxima corresponding to the measurement field orientation parallel and perpendicular, correspondingly, to the direction of the magnetic field applied during the sample preparation.

4. Conclusions

We studied the morphology, magnetization temperature dependences, and electron spin resonance (ESR) of $Cu_{1-x}Fe_xCr_2Se_4$ NPs ($x = 0$, 0.2, and 0.4) synthesized via the thermal decomposition of metal chloride salts and selenium powder with different ratios of the raw material components in a high-temperature organic solvent. According to the transmission electron microscopy data, NPs have a shape of thin nearly hexagonal plates. The plate thickness, 2d, and the lateral size, 2R, depend strongly on the x value. Both 2d and 2R are remarkably lower for $x = 0.4$. All the NPs are single crystalline with the $CuCr_2Se_4$ structure. The tendency is revealed of the nanoparticle consolidation into clusters of plates attached to each other "face to face". The Curie temperature, T_c, of the

powdered nanoparticle samples with $x = 0$ (410 K) is comparable to that presented in literature for $CuCr_2Se_4$ thin films and NPs. Introducing Fe into the particle composition affects in T_c decrease up to 322 K for $x = 0.4$. Two features were observed in the magnetization temperature dependences of the samples with $x = 0$ and 0.2. One of them appears as FC and ZFC bifurcation near 300 K and is associated with blocking of the particle magnetic moments. The other one appears as a kink near 130 K which is seen both in the FC and ZFC thermomagnetic curves. For the sample with $x = 0.4$, only the bifurcation of the FC and ZFC curves is observed due to the transition from the superparamagnetic to the blocked state.

The samples with $x = 0$ and 0.2 demonstrate the non-monotonous temperature dependence of the resonant field H_{res}. For the measurements in the X-band, the kink is observed at the same temperature for both compositions near 130 K; further temperature lowering affects in the H_{res} behavior similar to that observed for the $CuCr_2S_4$ NPs with the yield on the plateau near 50 K. The sample with $x = 0.4$ demonstrates only H_{res} decrease at the temperatures lower than the blocking temperature. ESR was also investigated in the higher frequency bands for two types of sample compacting: free particles, e.g., particles simply placed into a container and particles fixed with the glue. The peculiarities revealed in the ESR temperature dependences are shown to be due to the competition of the different nature anisotropies – in-plain shape anisotropy depending on temperature similar to the magnetization temperature dependence and the magnetocrystalline anisotropy increasing strongly with the temperature decrease. Being due to the redistribution of the contributions of the shape and magnetocrystalline anisotropies, the change of the interparticle magnetostatic interaction may also effect in the ESR characteristics temperature behavior.

Acknowledgements

The paper was partially supported by the President of Russia (Grant #NSh-7559.2016.2). We also thank the Ministry of Science and Technology of Taiwan, Taiwan, and the Siberian Branch of RAS, Russian Federation (MOST 102-2112-M-153-002-MY3) for the financial support.

References

[1] J.S. Bettinger, R.V. Chopdekara, M. Liberatic, J.R. Neulingere, M. Chshiev, Y. Takamura, L.M.B. Alldredgea, E. Arenholz, Y.U. Idzerda, A.M. Stacy, W.H. Butlerf, Y. Suzuki, J. Magn. Magn. Mater. 318 (2007) 65.
[2] H. Brandle, J. Schoenes, P. Wachter, F. Hulliger, W. Reim, Appl. Phys. Lett. 56 (1990) 2602.
[3] V.N. Antonov, V.P. Antropov, B.N. Harmon, A.N. Yaresko, A.Ya. Perlov, Phys. Rev. B 59 (1999) 14552.
[4] S. Bordacs, I. Kézsmárki, K. Ohgushi, Y. Tokura, New J. Phys. 12 (2010) 053039.
[5] F. Ogata, T. Hamajima, T. Kambara, K.I. Gondaira, J. Phys. C: Solid State Phys. 15 (1982) 3483.
[6] H. Hahn, C. de Lorent, B. Harder, Z. Anorg, Chem 283 (1956) 138.
[7] F.K. Lotgering, R.P. Van Stapele, J. Appl. Phys. 39 (1968) 417.
[8] I. Nakatani, H. Nose, K. Masumoto, J. Phys. Chem. Solids 39 (1978) 743.
[9] L. Zhang, W. Tong, J. Fan, C. Zhang, R. Li, Y. Zhang, Eur. Phys. J. B 83 (2011) 325.
[10] R. Li, Z. Qu, L. Zhang, L. Ling, W. Tong, Y. Zhang, Solid State Commun. 150 (2010) 2289.
[11] R. Li, C. Zhang, Y. Zhang, J. Magn. Magn. Mater. 324 (2012) 3133.
[12] T. Saha-Dasgupta, M. Raychaudhury, D. Sarma, Phys. Rev. B 76 (2007) 054441.
[13] S. Bedanta, W. Kleemann, J. Phys. D Appl. Phys. 42 (2009) 013001.
[14] K. Ramesha, R. Seshadri, Solid State Sci. 6 (2004) 841.
[15] Y. Aktas, O. Akman, M. Ozdem, Balkan, Phys. Lett. 16 (2009) 161053.
[16] C.-R. Lin, C.-L. Yeh, S.-Z. Lu, I.S. Lyubutin, S.-C. Wang, I.P. Suzdalev, Nanotechnology 21 (2010) 235603.
[17] D. Kim, A.N. Rusnak, S. Parameswaran, C.R. Patra, V.B. Trofimov, R. Harpness, A. Gedanken, Yu.S. Tver'yanovich, Glass Phys. Chem. 32 (2006) 330.
[18] Y. Wang, Q. Zhu, L. Tao, X.J. Su, Mater. Chem. 21 (2011) 9248.
[19] G.M. Tsoi, L.E. Wenger, Y.-H.A. Wang, A. Gupta, J. Magn. Magn. Mater. 322 (2010) 142.
[20] Yu.-Hsiang A. Wang, Ningzhong Bao, Liming Shen, Prahallad Padhan, Arunava Gupta, J. Am. Chem. Soc. 129 (2007) 12408.
[21] M.L. Rao, M. Shamsuzzoha, A. Gupta, J. Cryst. Growth 306 (2007) 321.
[22] B. Wang, H. Wu, L. Yu, R. Xu, T.T. Lim, X.W. Lou, Adv. Mater. 24 (2012) 1111.
[23] H.N. Ok, Yu Chung, Ju G. Kim, Phys. Rev. B 20 (1979) 4550.
[24] R.W.Q. Wyckoff, Crystal Structures, III, Wiley-Interscience, NY, USA, 1964, p. 78.
[25] M. Chevreton, Acta Crystallogr. A 16 (1963) 431.
[26] L. Morris, P. Russo, A. Wold, J. Phys. Chem. Solids 31 (1970) 635.
[27] K. Kojima, M. Matsui, K. Sato, K. Adachi, J. Phys. Soc. Jpn. 29 (1970) 1643.
[28] B.I. Min, S.S. Baik, H.C. Choi, S.K. Kwon, J.-S. Kang, New J. Phys. 10 (2008) 055014.
[29] R.D. Ivantsov, I.S. Edelman, S.M. Zharkov, D.A. Velikanov, D.A. Petrov, S.G. Ovchinnikov, C.-R. Lin, O. Li, Y.-T. Tseng, J. Alloy. Compd. 650 (2015) 887.
[30] M. Esters, A. Liebig, J.J. Ditto, M. Falmbigl, M. Albrecht, D.C. Johnson, J. Alloy. Compd. 671 (2016) 220.
[31] D. Du, F. Toffoletto, S.L. Biswal, Phys. Rev. E 89 (2014) 043306.
[32] M. Beleggia, S. Tandon, Y. Zhu, M. De Graef, J. Magn. Magn. Mater. 278 (2004) 270.
[33] A.I. Pankrats, A.M. Vorotynov, V.I. Tugarinov, S.M. Zharkov, D.A. Velikanov, G. M. Abramova, G.M. Zeer, K. Ramasamy, A. Gupta, J. Appl. Phys. 116 (2014) 054302.
[34] E. Schlomann, J. Phys. Chem. Solids 6 (1958) 257.